



# Development and Experimental Study of Disc Spring-Based Self-Centering Devices for Seismic Resilience

Cheng Fang, M.ASCE<sup>1</sup>; Wei Wang, M.ASCE<sup>2</sup>; and Deyang Shen<sup>3</sup>

**Abstract:** A novel self-centering device that employs disc springs as its kernel components is developed and experimentally verified in this study. The device is suitable for use in self-centering braced frames and is expected to provide a large initial stiffness, reliable self-centering capability, and satisfactory energy dissipation. The fundamental mechanical behavior of the new device is described first. The component detailing, working principle, and fabrication process are discussed in detail. This is followed by a series of tests on individual disc springs and friction plates to gain an in-depth understanding of the performance of these basic components. Subsequently, a full-scale device designed based on a prototype building is physically tested, and the reliability of the specimen under multiple earthquakes is further understood by carrying out repeated rounds of cyclic loading. Among other findings, it is observed that the proposed device has excellent self-centering capability with equivalent viscous damping (EVD) of up to 36%. The device can provide sufficient deformability, corresponding to an available interstory drift of at least 4%. The device is capable of withstanding multiple rounds of loading with no degradation, highlighting its superiority for use against sequential strong earthquakes with no need to replace/repair. The analytical expressions are validated through comparisons against the test results, and a parametric study is then conducted to examine the effects of some key design factors on the device behavior. Based on the experimental and analytical studies, some practical design recommendations are finally given. DOI: 10.1061/(ASCE) ST.1943-541X.0003058. © 2021 American Society of Civil Engineers.

**Author keywords:** Self-centering; Disc spring; Earthquake; Seismic resilience; Friction; Braced frame.

## Introduction

Peak interstory drift and absolute floor acceleration have been recognized as essential indices for the evaluation of structural and nonstructural seismic performances of building structures. As performance-based seismic design (PBSD) prevails, one other possible metric that has attracted significant attention is the residual interstory drift (Erochko et al. 2011). Complementing the existing performance indices, residual interstory drift is the permanent deformation of a structure seeing an earthquake, and it indirectly indicates the potential damage to the members and systems. According to McCormick et al. (2008), who conducted a field investigation in Japan after the 1995 Kobe earthquake, residual interstory drifts exceeding 0.5% are generally unacceptable, and in addition, reconstruction becomes more economically feasible than repairing a damaged structure when the residual interstory drift is larger than 0.5%. The urgent need for considering seismic resilience was reemphasized after the 2011 Christchurch earthquake in which hundreds of noncollapsed buildings with significant damages and

residual deformations were demolished, leading to a total economic loss of NZD 40 billion, making up almost 20% of the country's annual gross domestic product (GDP) (Wood et al. 2016).

While establishing a resilient city requires sustained efforts from various sectors (e.g., construction, finance, society, health, and so forth), structural resiliency is still one of the most effective and critical elements toward this goal (Jiang et al. 2019; Zhang et al. 2020). The term structural resiliency involves various meanings, among which *self-centering*, indicating practically negligible residual interstory drifts after an earthquake, is one of the most promising strategies. Self-centering capability can be achieved by rocking behavior, which permits the structure to uplift and largely remain elastic during seismic excitations (Wu et al. 2018). Extra energy dissipators (EDs) are provided to prevent overly large roof drifts. Another approach was to endow beam-to-column connections with self-centering capabilities, a solution which is realized by posttension (PT) reinforcement/tendons placed along the beam (Ricles et al. 2001, 2002; Lin et al. 2013; Dimopoulos et al. 2013; Latour et al. 2019). It was later found that the gap opening mechanism could cause a detrimental *beam-growth* or *frame expansion* effect, which causes deformation incompatibility of the frame and significant damage to the floor diaphragm. Many follow-up studies have been carried out to try to solve this problem (Garlock and Li 2008; Chou and Chen 2011a, b; Feng et al. 2019; Fang et al. 2019a).

Alternatively, self-centering braces have been proposed, which may be more easily accepted by the industry due to the advantages of fast installation (the elimination of field pretensioning), easier commercialization, and being free from the beam-growth effect (Tremblay et al. 2008; Zhu and Zhang 2008; Huang et al. 2018). Inspired by the basic concept of self-centering connections with PT-tendons, Christopoulos et al. (2008) successfully verified a pioneering type of PT tendon-based self-centering brace that exhibited recoverable tensile and compression deformations. The braces were

<sup>1</sup>Associate Professor, State Key Laboratory of Disaster Reduction in Civil Engineering, Dept. of Structural Engineering, Tongji Univ., Shanghai 200092, China. Email: chengfang@tongji.edu.cn

<sup>2</sup>Professor, State Key Laboratory of Disaster Reduction in Civil Engineering, Dept. of Structural Engineering, Tongji Univ., Shanghai 200092, China (corresponding author). ORCID: <https://orcid.org/0000-0003-1241-465X>. Email: weiwang@tongji.edu.cn

<sup>3</sup>Graduate Student, Dept. of Structural Engineering, Tongji Univ., Shanghai 200092, China. Email: 1732510@tongji.edu.cn

Note. This manuscript was submitted on July 13, 2020; approved on February 24, 2021; published online on April 27, 2021. Discussion period open until September 27, 2021; separate discussions must be submitted for individual papers. This paper is part of the *Journal of Structural Engineering*, © ASCE, ISSN 0733-9445.

updated to provide larger load-carrying capacities (Erochko et al. 2015a) and were dynamically tested via a shaking table (Erochko et al. 2013). However, one practical problem for such braces is the limited deformability of the PT tendons, noting that a high-strength steel tendon typically has an elastic deformation capacity of 0.5%–1.5%. As a result, the maximum peak interstory drift that the braces can provide is limited, depending on the effective length of the tendon, bracing angle, and required prestressing. Chou et al. (2014, 2016) and Erochko et al. (2015b) further proposed dual-core braces that alleviate this problem to a certain extent, although the maximum deformability could still be lower than the deformation demand of the structure under strong or pulse-like near-fault earthquakes (Fang et al. 2018). In addition, the system-level analysis showed that although the emerging system could significantly reduce the residual deformation without necessarily increasing the maximum deformation compared with conventional yielding systems (Moradi et al. 2014), increased peak floor acceleration and a detrimental high-mode effect could be induced if the energy dissipation capability is insufficient (Qiu and Zhu 2016). This highlights the necessity of providing adjustable energy dissipation sources in self-centering frames; in other words, a balance between self-centering capability and energy dissipation should be maintained in practical designs (Tremblay et al. 2008; Kari et al. 2011; Eatherton et al. 2014). This issue is particularly addressed in this study by proposing a new self-centering device with tunable hysteretic shapes. More recently, a unique class of smart metals called shape memory alloys (SMAs) has been introduced for self-centering members (Fang et al. 2014, 2015a, b, 2017; Wang et al. 2016, 2017a, b; Qiu and Zhu 2017a, b; Yam et al. 2015; Miller et al. 2012; Xu et al. 2016b; Farmani and Ghassemieh 2017; Chowdhury et al. 2019; Ke et al. 2020). The superelasticity of the material provides a spontaneously recoverable strain of 8%–10%, which significantly enhances the deformability of self-centering braces. While many studies have been conducted on this front, practical concerns related to cost and temperature sensitivity may need to be further clarified before the material can be confidently used in the construction industry.

In contrast to the PT tendon solution in which the deformability is restricted by the length of the tendon, alternative mechanical components, such as friction springs or disc springs, can serve the same purpose with much more flexible properties (Khoo et al. 2012, 2013; Ramhormozian et al. 2017, 2019; Hashemi et al. 2019). The main design concept is to develop a special device/damper that accommodates and always compresses these springs when the device is subjected to either tension or compression. Some researchers (Wang et al. 2019a, b; Fang et al. 2019b) developed a self-centering device employing friction springs. A friction spring group consists of a series of outer and inner rings assembled alternately with tapered mating surfaces and typically has large load resistance accompanied by considerable energy dissipation due to the friction between the outer and inner rings. Xu et al. (2016a, 2017a, b, 2020) conducted a series of tests on alternative self-centering devices equipped with disc springs. Stable flag-shaped hysteretic responses were obtained, and a maximum deformation capacity of 25 mm was achieved. Dong et al. (2017) endowed buckling restrained braces (BRBs) with self-centering capability by introducing an extra set of disc springs. The brace failed in multiple-wave buckling of the steel core of the BRB, and the maximum considered displacement was 20 mm. Some other novel types of self-centering devices have also been proposed (Kitayama and Constantinou 2017; Tong et al. 2019; Bagheri et al. 2020).

Compared with the substantial body of literature on PT tendon-based self-centering members, test evidence on the spring-based solutions, especially full-scale devices, is still very limited. This paper presents an experimental study on a new type of self-centering

device equipped with disc springs working together with friction EDs. The new device is easy to assemble and has a large initial stiffness, adjustable yield strength and deformability, excellent self-centering capability, and satisfactory energy dissipation, making it an ideal option for self-centering braced frames. The study commences with a detailed description of the working mechanism of the proposed device, followed by cyclic tests on individual disc springs and friction EDs, both of which are kernel elements of the device. Particular interest is given to different candidates of friction materials, fostering a better understanding of their mechanical performance and reliability. A full-scale self-centering device, aiming to provide an interstory drift of at least 4% for a predesigned steel braced frame, is produced and tested. The fabrication process of the device is elaborated, and the test results are discussed in detail. Preliminary design recommendations are also given based on the available test data.

## Working Principle of Proposed Device

### Disc Springs

Disc springs are mechanical components commonly used for bolt looseness prevention and impact buffering. The geometric configuration of a typical disc spring can be characterized by the following parameters: external and internal diameters ( $D$  and  $d$ ; defining  $C = D/d$ ), height ( $H_0$ ), and thickness ( $t'$ ), as illustrated in Fig. 1(a). A group of disc springs can be used with different stack combinations, i.e., in series or in parallel, to achieve flexible deformability and load resistance. Compared with other types of springs, such as helical or friction springs, the disc springs are more stable due to their flat annular conical shape and concentric force transmission. For a disc spring with the geometric configuration, shown in Fig. 1(a), the relationship between the load resistance  $F$  and the compressive deformation  $f$  can be expressed by [GB/T 1972–2005 (Chinese Standard 2005)]

$$F(f) = \frac{4E}{1-\mu^2} \times \frac{t'^4}{K_1 D^2} \times K_4^2 \times \frac{f}{t'} \left[ K_4^2 \left( \frac{h'_0}{t'} - \frac{f}{t'} \right) \left( \frac{h'_0}{t'} - \frac{f}{2t'} \right) + 1 \right] \quad (1)$$

where  $E$  = Young's modulus of the material;  $\mu$  = Poisson's ratio; and  $h'_0$  = maximum deformation capacity of each disc spring, as expressed

$$h'_0 = H_0 - t' \quad (2)$$

Other parameters can be obtained by the following equations:

$$K_1 = \frac{1}{\pi} \times \frac{[(C-1)/C]^2}{(C+1)/(C-1) - 2/\ln C} \quad (3)$$

$$K_4 = \sqrt{-\frac{C_1}{2} + \sqrt{\left(\frac{C_1}{2}\right)^2 + C_2}} \quad (4)$$

$$C_1 = \frac{(t'/t)^2}{((5/8) \times (H_0/t) - t'/t + 3/4)[(5/8) \times (H_0/t) - t'/t + 3/8]}, \quad t'/t = 0.94 \quad (5)$$

$$C_2 = \frac{C_1}{(t'/t)^3} \left[ \frac{5}{32} \left( \frac{H_0}{t} - 1 \right)^2 + 1 \right] \quad (6)$$

The tangent stiffness of the disc spring is given

$$K(f) = \frac{4E}{1-\mu^2} \times \frac{t'^3}{K_1 D^2} \times K_4^2 \left\{ K_4^2 \left[ \left( \frac{h'_0}{t'} \right)^2 - 3 \times \frac{h'_0}{t'} \times \frac{f}{t'} + \frac{3}{2} \left( \frac{f}{t'} \right)^2 \right] + 1 \right\} \quad (7)$$

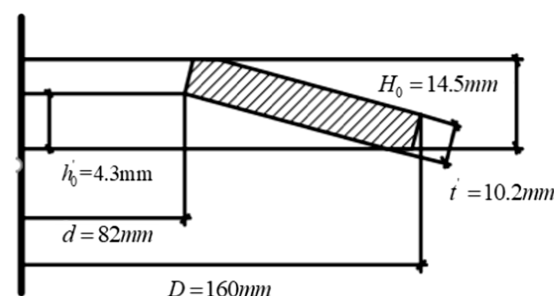
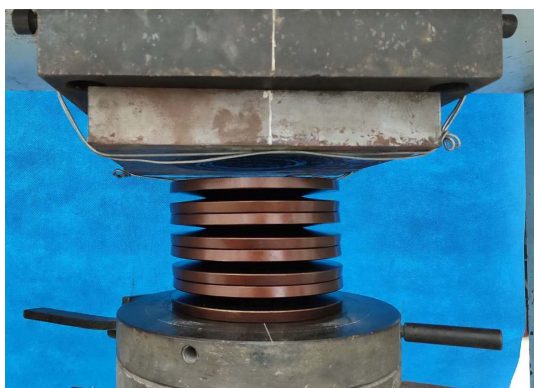
Fig. 1(b) compares the test result of a typical disc spring (or disc spring group) with the analytical prediction in which good agreements are found in terms of the stiffness. The slight hysteretic loops exhibited by the disc springs during the cyclic loading were mainly attributed to the extra friction between the disc spring and the supporting surfaces.

### Details and Analytical Expression of Proposed Device

As shown in Fig. 2(a), the proposed device mainly consists of an internal shaft (used together with a sleeve), an external tube (including two parts that are later assembled via a threaded junction), a guiding tube, a friction ED, a group of disc springs, and other necessary accessories, such as shim plates, ear plates, tightening nuts, and high-strength bolts. The disc springs pass through the internal shaft and are firmly confined within the device. Preload to the disc springs should be applied and maintained by the sleeve and tightening nuts. In this way, the precompressed disc springs could

provide a desirable yield resistance for the device. The guiding tube is used to make sure that the disc springs keep aligned and only deform and move axially. The friction ED is separated from the disc springs after earthquakes—a case that allows easy inspection and replacement if necessary. The energy dissipation is provided by the friction interface between the friction pads (which move together with the internal shaft through the high-strength bolts) and the extended part of the external tube.

Fig. 2(b) illustrates the deformation mode of the proposed device. Any relative movement between the internal shaft and the external tube leads to compression of the disc springs, and as a result, a tension-compression equally functioned device is enabled. In particular, when the device is in compression, the internal shaft along with the sleeve pushes down the disc springs (see the orientation of the figure), while the bottom end of the disc spring group is supported by the stepped section of the external tube. At the same time, the friction plates move down together with the internal shaft, enabling a relative movement against the extended part of the external tube. In other words, friction is induced over the interface between the friction plate and the polished flat surface of the external tube. Similarly, when the device is in tension, the internal shaft along with the tightening nuts push up the disc spring group, which is supported by the external tube at the other end. Again, the relative movement between the internal shaft (together with the friction plate) and external tube causes friction. During this process, the



(a)

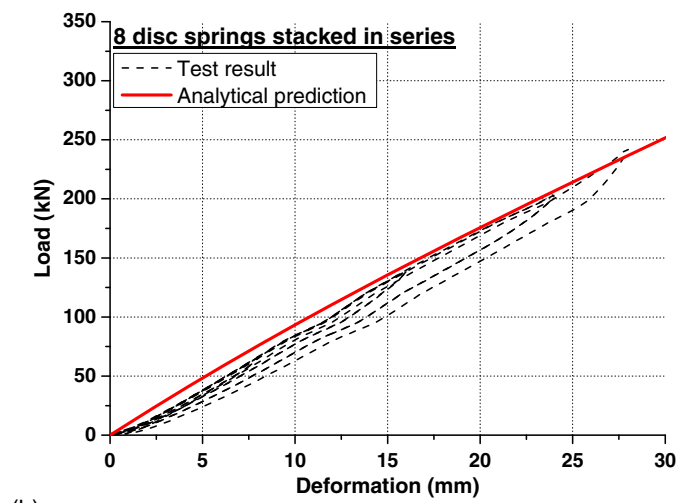
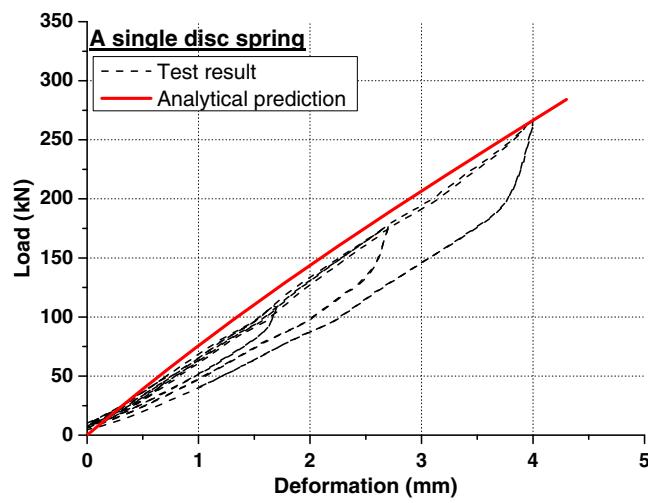
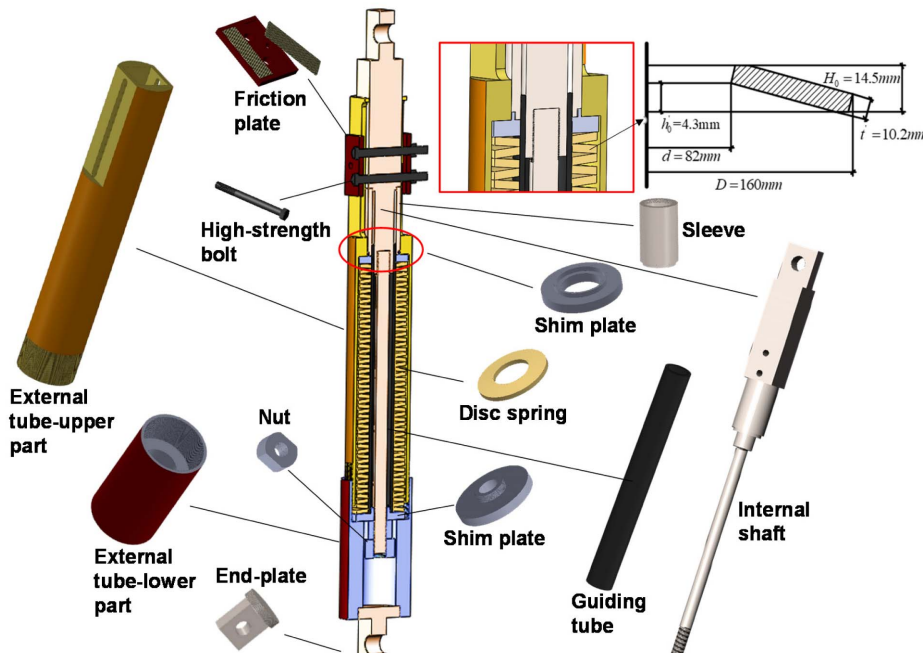


**Fig. 1.** Test of disc springs: (a) geometric configuration and dimension (not to scale); and (b) load-deformation response.



(a)

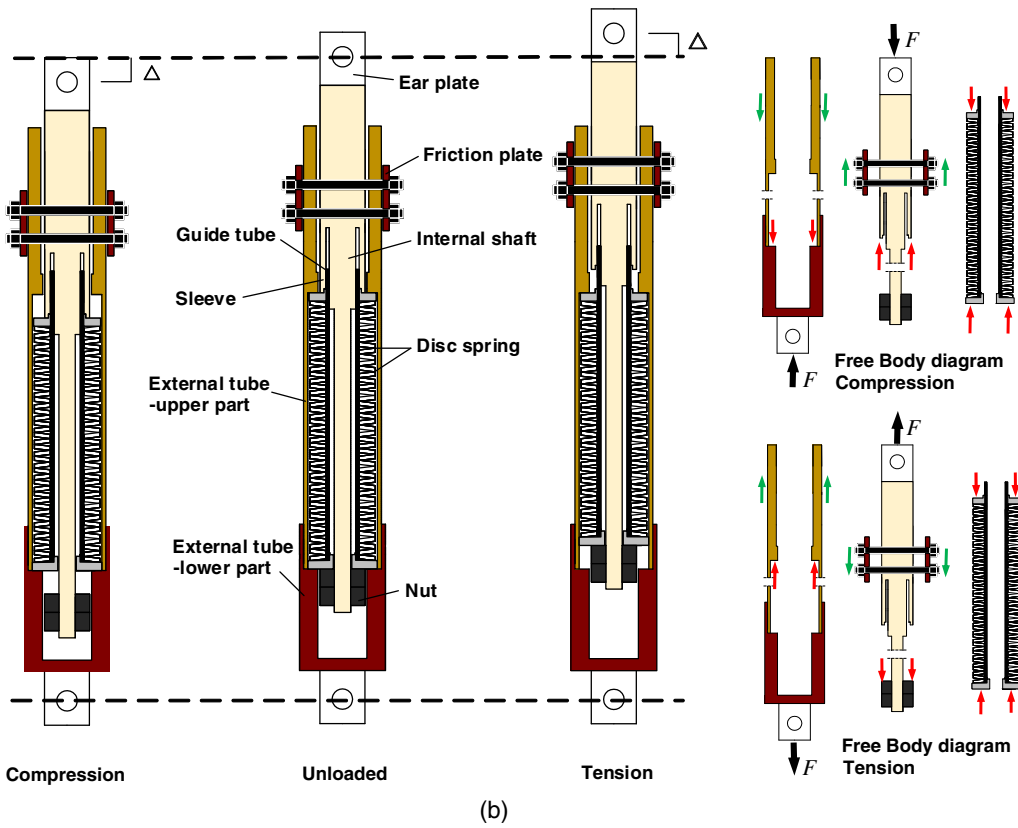


**Fig. 2.** Proposed self-centering device: (a) basic components; and (b) working principle and free body diagram.

guiding tube only serves as a lateral constrainer for the disc springs and should move freely within the void between the internal shaft and the sleeve.

When the precompressed disc springs act together with the friction ED, the entire device is expected to exhibit a flag-shaped hysteretic behavior, as shown in Fig. 3. The yield strength  $F_y$  is the

sum of the preload of the disc spring group ( $F_p$ ) and the frictional force ( $F_f$ ). The former is converted from the predeformation of the disc spring group using Eq. (1); the latter depends on various factors, such as the friction material, steel plate surface treatment, and bolt torque. The theoretical initial stiffness  $K_i$  of the device may be expressed

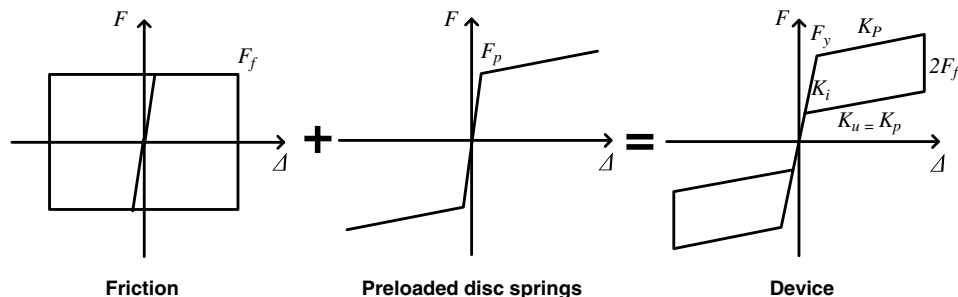


**Fig. 3.** Illustration of the load-deformation response of proposed device (not to scale).

$$\frac{1}{K_i} = \frac{1}{K_{in}} + \frac{1}{K_{e-u}} + \frac{1}{K_{e-l}} \text{ in tension} \quad (8)$$

$$\frac{1}{K_i} = \frac{1}{K_s} + \frac{1}{K_{e-l}} \text{ in compression} \quad (9)$$

where  $K_{in}$ ,  $K_{e-u}$ ,  $K_{e-l}$ , and  $K_s$  are the axial stiffnesses of the internal shaft, external tube-upper part, external tube-lower part, and sleeve, respectively. In fact, an accurate prediction of  $K_i$  is a big challenge due to the unpredictable sources of uncertainty and imperfections, as discussed subsequently. In practice, the initial stiffness may be determined by sample testing. This can be considered as a standard quality control procedure, which is now widely adopted for commercial BRB and other damper products. The postyield stiffness  $K_p$  is equal to the loading stiffness of the disc spring group [Eq. (7)]. During unloading, friction reversal first leads to a sudden drop of the load resistance in which the decrease is equal to  $2F_f$ . The stiffness of the unloading plateau  $K_u$  should be the same as  $K_p$ .

### Recommended Fabrication Process

To make the device perform as intended, a special fabrication/assembly process is recommended, as illustrated in Fig. 4. A simple

workstation together with a temporary base block can be used as the foundation. A shim plate is first placed on the base support where the lateral movement of the shim plate is prevented; then, the guiding tube is installed, which stands vertically on the shim plate (Step 1). The disc springs are then installed one by one, and the guiding tube, which passes through these disc springs, serves as an internal constraint to prevent lateral movement of the disc springs (Steps 2 and 3). Different combinations of the disc springs can be adopted as needed. Another shim plate is placed on the top of the disc springs (Step 4), and subsequently, the internal shaft is installed by passing through the guiding tube (Step 5). As mentioned, a sleeve is used that transfers the load from the internal shaft to the top shim plate. The temporary base block is then removed, and the tightening nuts are screwed. Two approaches can be used to apply the necessary preload to the disc springs: one is to compress the disc springs by directly tightening the nuts, and the other is to compress the springs via an actuator and then screw the nut manually. While the former approach is easier to realize as it requires no additional loading facility, compressing a disc spring group with a large load carrying capacity (e.g., thousands of kilonewtons) can be difficult. The latter approach, which was adopted in the current study, is more suited to heavy devices. After the preload is applied, the two parts of the external tube are assembled (Steps 6 and 7). The friction

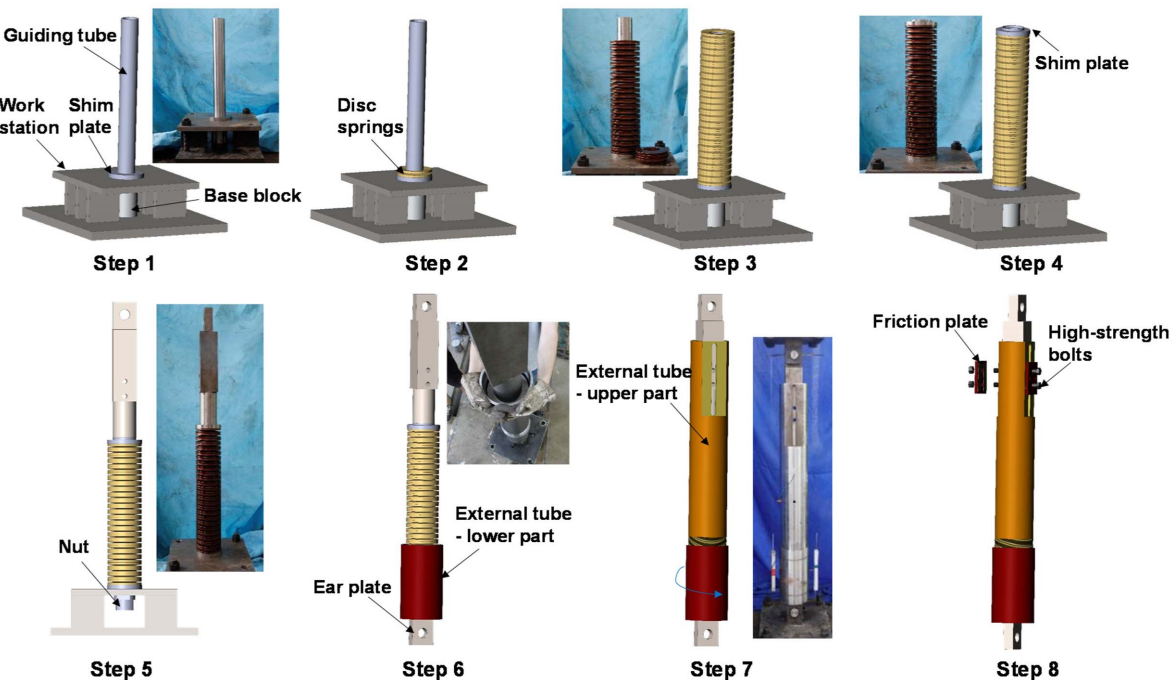


**Fig. 4.** Recommended fabrication steps for the device.

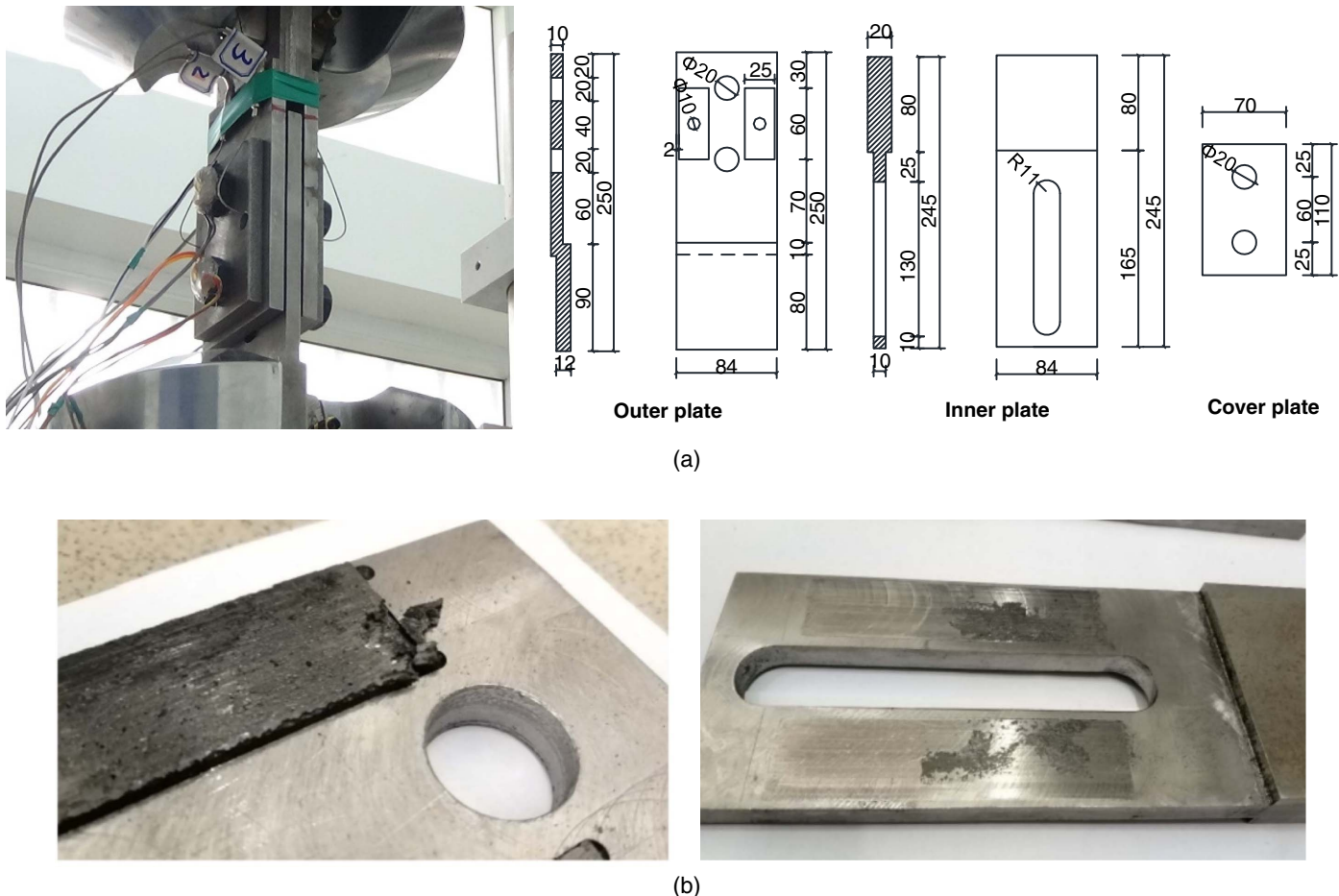


**Fig. 5.** Individual friction EDs: (a) test setup; and (b) observations after the test.

EDs are finally installed, and the high-strength bolts are tightened to exert the required normal pressure (Step 8).

## Tests on Friction EDs

### Test Arrangement

Tests on individual friction EDs were carried out to examine the hysteretic behavior of different friction material-steel interfaces and to select an appropriate friction material for the self-centering device. Three friction material candidates were considered, namely, nonasbestos carbon fiber composite (NCFC), nonasbestos aramid fiber composite (NAFC), and nonasbestos calcium sulfate whisker composite (NCSWC). The friction pads made of these composite materials were embedded in the recesses made on the contacting surfaces of the outer Q345 (nominal yield strength = 345 MPa) steel plates such that the relative movement between the friction pads and the recessed steel plates was physically restricted. The normal pressure was applied by tightening the two high-strength bolts to the required preload, which was controlled by a torque wrench. The test setup is illustrated in Fig. 5(a). The maximum torque was 250 Nm, corresponding to a theoretical bolt force of 58.5 kN.

A total of six tests were conducted, and the main testing parameters are given in Table 1. For each friction material, two levels of bolt preload were considered, corresponding to two different normal pressures. New friction pads were used for each test, i.e., the

**Table 1.** Details and key results of tests on individual friction EDs

Test number	Friction material	Torque of bolt (Nm)	Static friction coefficient	Dynamic friction coefficient	Abrasion ratio (%)	Temperature increase (°C)
1	NCFC	100	0.30	0.18–0.34	0.53	+17
2	NCFC	250	0.29	0.16–0.30	0.78	+37
3	NAFC	100	0.18	0.17–0.42	0.62	+22
4	NAFC	250	0.19	0.18–0.47	0.71	+47
5	NCSWC	100	0.21	0.18–0.34	0.31	+34
6	NCSWC	250	0.25	0.21–0.36	0.41	+43

friction material was not used repeatedly for the different tests. A constant amplitude of  $\pm 20$  mm with a loading rate of 1 mm/s was adopted, and 100 cycles were repeated for each test. To measure the variation of the temperature during the tests, a thermal couple was placed on the backside of the friction pad through a preopening cut on the steel plate. In addition, the bolt strain was monitored via a pair of strain gauges mounted on the shank part of the bolt. The strain gauge reading  $\varepsilon$  could be easily converted to the normal pressure  $P_F$  by the following equation:

$$P_F = \sum \varepsilon E A_b \quad (10)$$

where  $E$  = Young's modulus of steel;  $A_b$  = cross-sectional area of each bolt; and  $\Sigma$  = total number of the prestressed bolts.

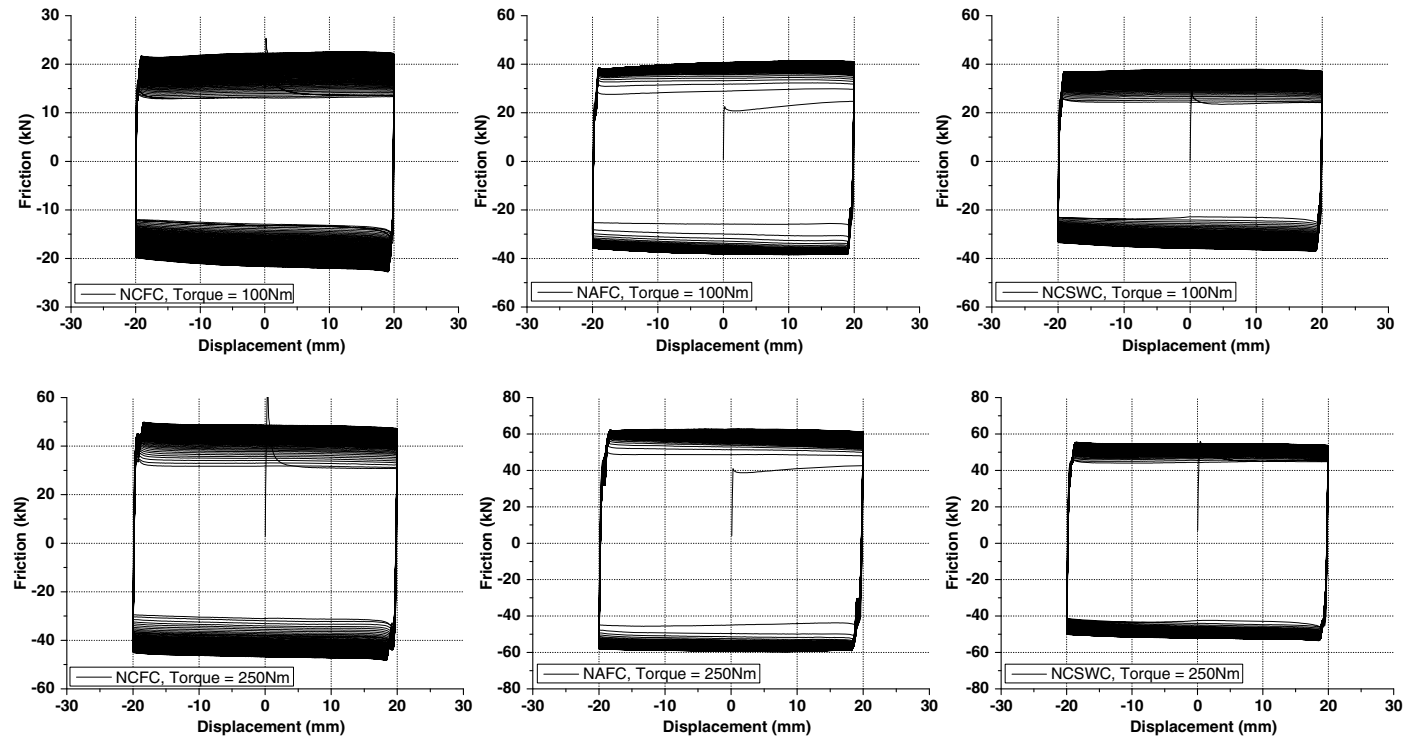


**Fig. 6.** Hysteretic curves of individual friction EDs.

## Test Results

The hysteretic curves of the six individual friction EDs are shown in Fig. 6. While the different friction materials exhibit varied hysteretic responses, the frictional force generally increases (by up to 50%) with increasing cycles. This tendency could be attributed to the abrasion of the friction material and, hence, the rougher surface of the friction pad. It is also found that the hysteretic loops become stabilized as the cycle is accumulated. The typical bolt axial forces are shown in Fig. 7(a). The bolt force keeps decreasing, which could be explained by the abrasion of the friction material, i.e., the thickness of the friction pad decreases. This also indicates that the normal pressure decreases with increasing cycles. The static and dynamic friction coefficients, as summarized in Table 1, can be derived from dividing the frictional force (considering double shear) by the normal pressure. Being consistent with the trend of the frictional force, the dynamic friction coefficient gradually increases, with a maximum value of around 0.43 observed for the NAFC-to-steel interface. In addition, the thermal couple shows that the temperature of the friction material keeps rising as the cycle is accumulated, as typically shown in Fig. 7(b). A larger normal pressure leads to a more significant temperature rise in which the maximum increase is 50°C. The variation of temperatures might also have a certain influence on the friction property.

The friction EDs were dismantled for further inspection after the tests. As shown in Fig. 5(b), the friction pads all kept in one piece, although in some cases, the surface was partially damaged. The abrasion ratio is calculated by comparing the thicknesses of the friction pad before and after the tests using a micrometer. As given in Table 1, the abrasion ratio ranges between 0.31% and 0.78%. The steel surface also exhibited minor abrasion. Compared with the other two friction materials, the NAFC friction pad leads to more stable hysteretic curves and the largest friction coefficient. Therefore, NAFC was used consistently for the proposed self-centering device.

## Tests on Self-Centering Device

### Test Specimen

A full-scale test specimen was designed based on a six-story prototype steel building frame, as shown in Fig. 8(a). The structure was assumed to locate on a stiff soil site (Site Class D) in Los Angeles and was designed based on ASCE/SEI 7-16 (ASCE 2016). The span and the height of the braced bay are 6 and 3.3 m, respectively, and each device in the brace is expected to provide a stroke of at least 90 mm, corresponding to an interstory drift of 4%. The required strengths for the different floors are different, so the necessary size and combination pattern of the disc springs vary on different floors. The current test specimen was extracted from the 6th floor, where the required tributary interstory shear is 420 kN, corresponding to an axial yield resistance of around 150 kN ( $1.414 \times 420/4$ ) for each diagonally-placed device.

Based on the required strength and deformation, appropriate disc springs were selected in which the basic dimensions are shown Fig. 1(a). Each individual disc spring can provide a theoretical maximum load resistance of 284 kN at a maximum deformation of 4.3 mm when flattened; although in practice, full utilization of this available deformation is not recommended [GB/T 1972–2005 (Chinese Standard 2005)]. A total of 50 disc springs were used in the current device, and they were all stacked in series. This combination allows a total maximum deformation capacity of 215 mm, among which 65 mm was later consumed for preloading (determined according to the required yield resistance), and the remaining was used for axial deformation. The maximum load resistance of the disc spring group is the same as that of a single spring. NAFC friction pads together with two grade 10.9 M22 high-strength bolts were used for providing energy dissipation. Based on a preliminary calculation, the torque applied to each bolt was determined to be 540 Nm such that a full self-centering capability is just achieved. The disc springs were produced from 60Si2Mn steel, and 40Cr and

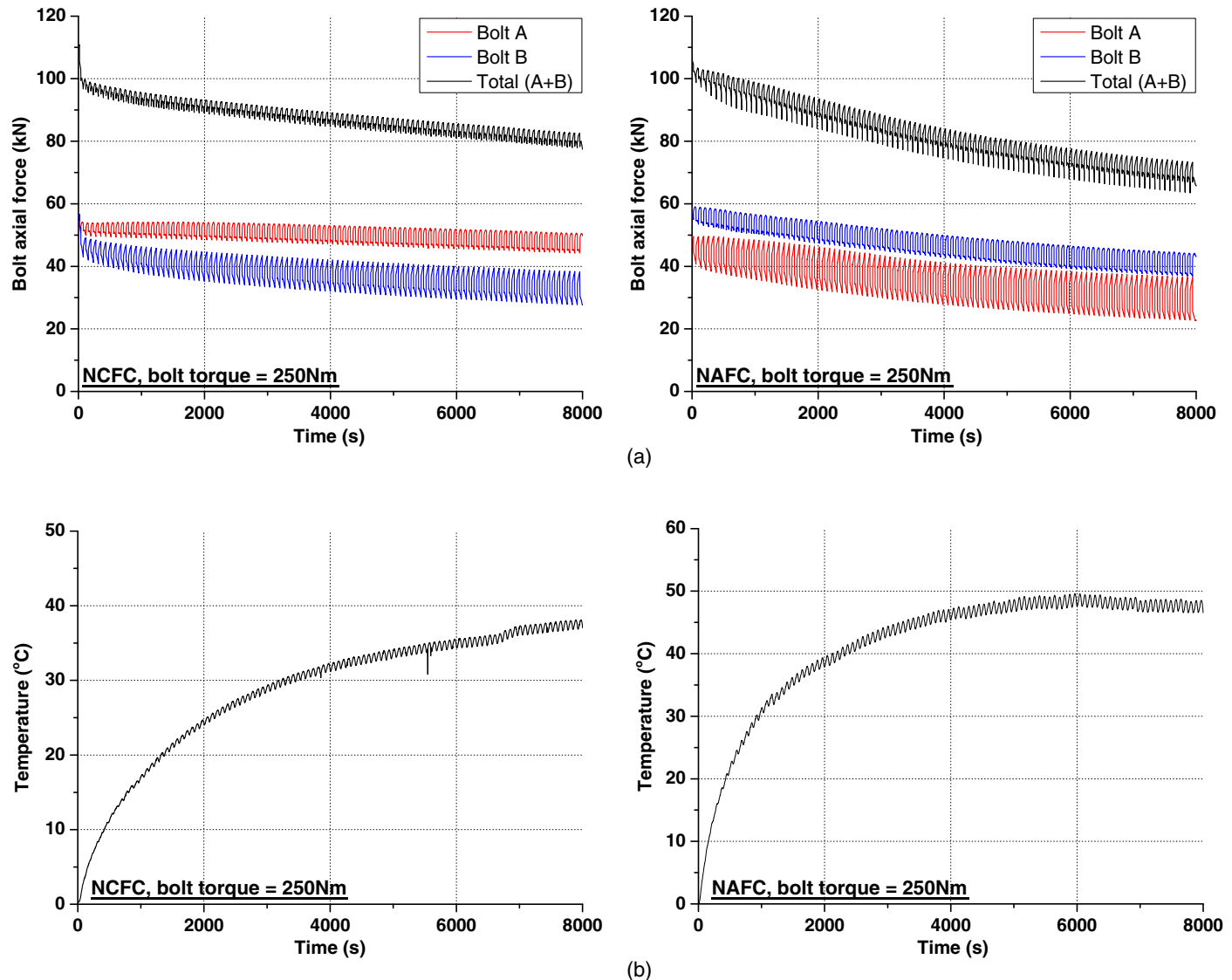


**Fig. 7.** Monitoring of friction component tests: (a) variation of bolt axial force; and (b) variation of temperature.

45# steel were used for the internal shaft and the other components of the device, respectively.

The dimensions of the main parts of the device were determined according to the following basic rules: (1) the strengths of the internal shaft, external tube, and other accessories are significantly larger than the maximum possible load resistance of the disc spring group plus the frictional force; (2) the length of the external tube was determined to accommodate a stroke of at least 90 mm; and (3) all the threaded regions were designed to have a strength larger than the maximum possible force experienced by the device. The geometric details of the device specimen are shown in Fig. 8(b). For ease of identification, this device is named Specimen SC-F.

#### Test Setup and Instrumentation

The test setup was designed to examine the performance of the self-centering device under axial cyclic loading. As shown in Fig. 9, the two ends of the specimen were connected to the actuator and strong floor beam via plain hinges. The SAC loading protocol, which considers interstory drift as the governing parameter, was adopted. The interstory drifts were converted to the axial displacement through

the corresponding geometric relationship. The loading amplitude started from 8.44 mm (0.375% interstory drift) and terminated at 90 mm (4% interstory drift), as shown in Fig. 9. Instead of six repeated cycles at small amplitudes required by the SAC loading protocol, only two cycles were conducted at each amplitude to reduce the test time. Nevertheless, three repeated rounds of cyclic loading (i.e., the entire loading protocol was repeated three times) were carried out to examine the behavior of the device under possible sequential earthquakes. Subsequently, the friction pads were removed, and the device was retested twice using the same loading protocol (subsequently named Specimen SC-0, in comparison to Specimen SC-F with the friction ED). This additional test aimed to quantitatively understand the contributions from the disc springs and friction ED to the load resistance and energy dissipation.

The axial deformation of the device was measured by a pair of vertical LVDTs attached to the upper ear plate of the internal shaft as well as the bottom part of the external tube. This arrangement could exclude irrelevant sources of deformation, such as that induced by the possible minor clearance of the plain hinges, from the measurement. A pair of strain gauges were mounted on the surface of the external tube to check if the load was applied concentrically.

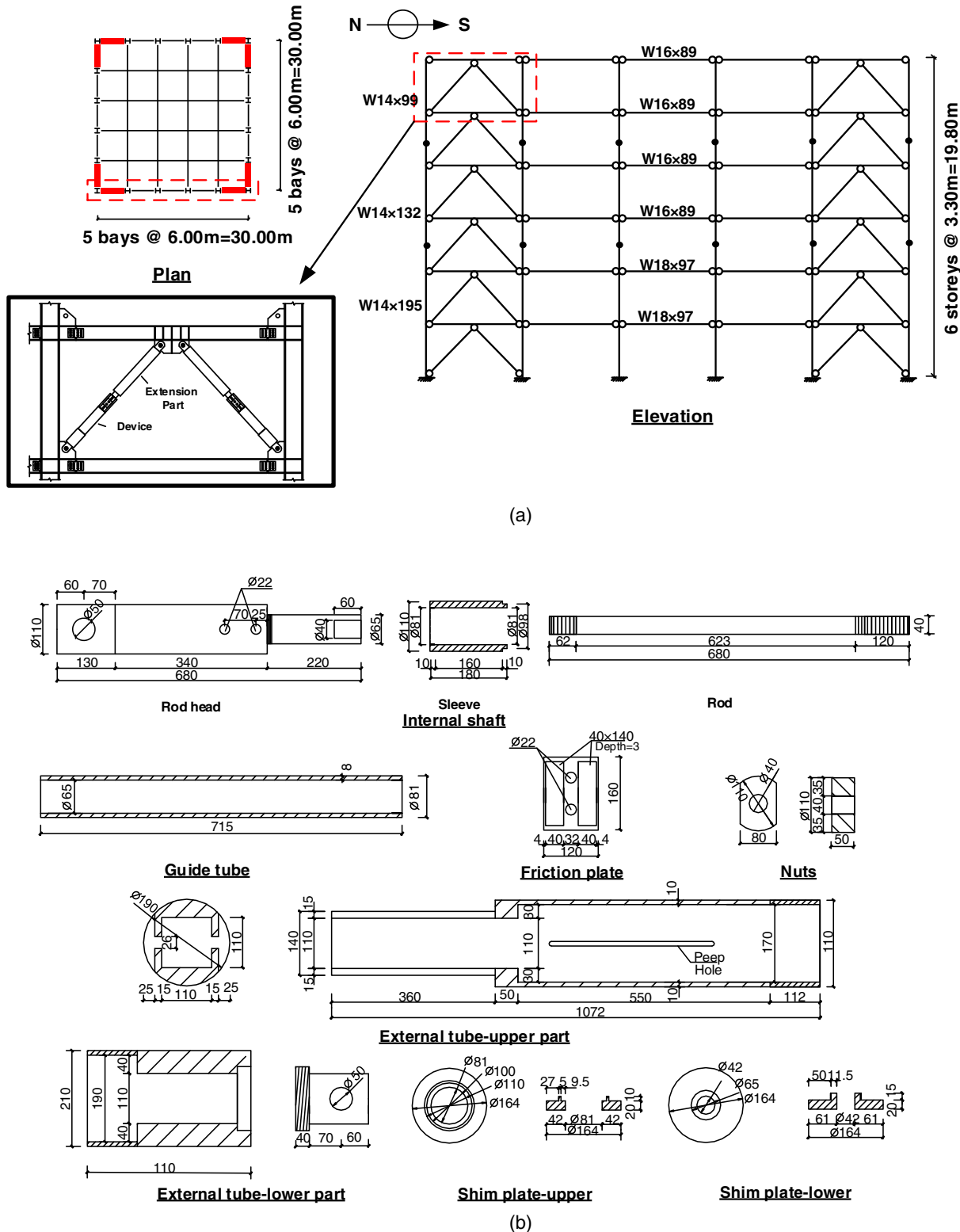


**Fig. 8.** Device specimen: (a) prototype building; and (b) geometric details.

The strain gauge readings were also used to confirm that the component kept elastic during the loading process. In addition, the axial strain of the high-strength bolts that provided the friction was measured to ensure that an intended bolt preload was applied. Two vertical openings were made on the external tube to facilitate the observation of the disc springs.

### Test Results

The overall behavior of the self-centering device was consistent with the design expectation. As typically shown in Fig. 10, the disc springs were compressed (i.e., the gap width between the disc springs was decreased) when the device was loaded. The disc springs were not fully flattened, which means that the device could

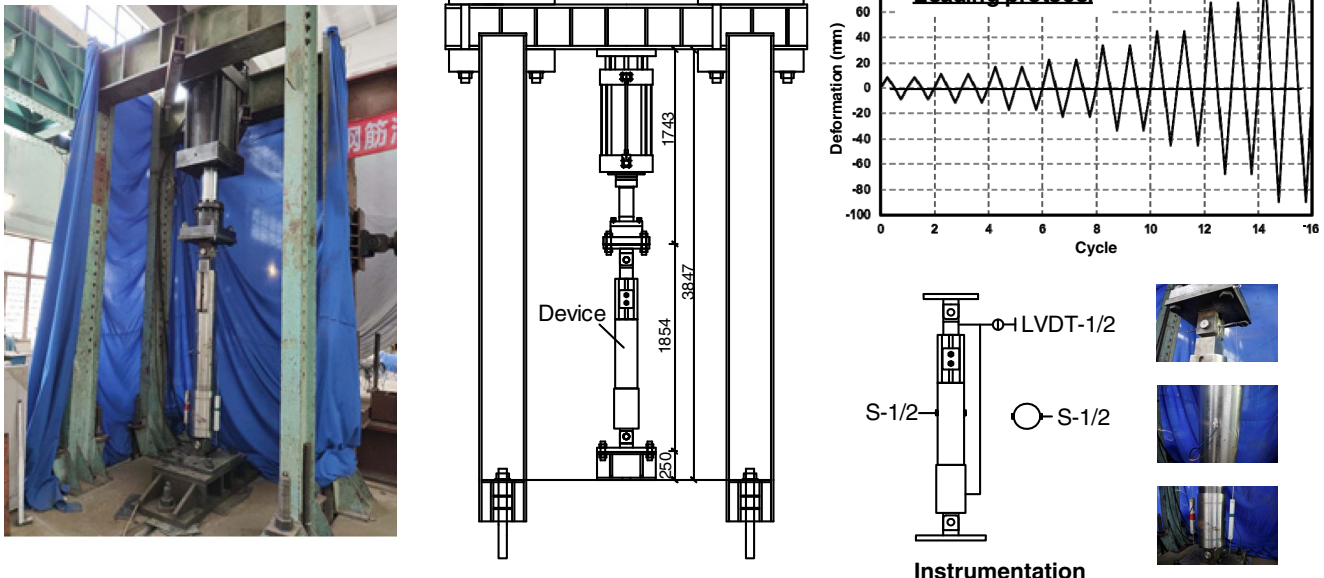


**Fig. 9.** Test setup and instrumentation for device specimen.

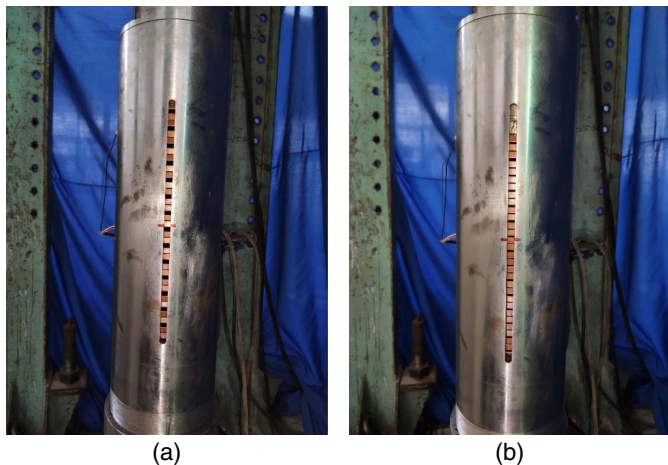


**Fig. 10.** Condition of disc springs at typical loading stages: (a) after precompression; and (b) 90 mm in compression.

still accommodate further deformation beyond  $\pm 90$  mm, although no such attempt was made in the present test program. This available margin for further deformation could be considered as a reservation for unexpectedly large deformation demands under an event beyond the maximum considered earthquake (MCE).

The relative movement between the internal shaft (together with the friction pads) and the external tube was attributed to the friction action. The behavior of the device under the repeated rounds of cyclic loading appeared to be the same. After completing the necessary rounds of loading, the device was dismantled for a detailed inspection. It was found that the main components, including the friction pads and disc springs, generally stayed intact, implying that the proposed device was fully reusable and insensitive to repeated loading. Therefore, the device is expected to survive sequential earthquakes without needing to be replaced.

The stable performance of the device could be further confirmed by examining the load-deformation hysteretic curves, as shown in

**Fig. 11.** Fig. 11(a) gives the results of the specimen equipped with the friction ED (Specimen SC-F). No visible difference is seen under the three repeated rounds of cyclic loading. The load-deformation curve first follows a linear ascending curve with large initial stiffness. This high-stiffness characteristic is attributed to the preloaded status of the disc springs before activation (decompression) and is of critical importance for the application of the device in braced frames. A yield resistance of approximately 150 kN is then achieved, which is followed by a loading plateau with a certain hardening slope. As mentioned, the yield resistance is contributed by the preload of the disc springs plus the frictional force provided by the friction ED, and the postyield stiffness is largely related to the linear stiffness of the disc spring group after activation. Upon unloading, the presence of the friction causes a parallelogram-shaped hysteresis. Excellent self-centering capability with a reasonably wide hysteresis and negligible residual deformation is exhibited.

It is also noticed that the hysteretic curve is not fully symmetrical. The load resistance and the width of the hysteresis in compression are slightly larger than those properties in tension. Such behavior is caused by the unexpected friction between the sleeve and the guiding tube, in which the latter was supposed to move freely within the void between the internal shaft and the sleeve, but in real cases, extra friction was induced because the void was not properly designed. According to Fig. 2(b), the friction-induced in the void is more significant when the device is in compression. Fig. 11(b) gives the test results of the device after removing the friction ED (SC-0). Again, the minor hysteresis is due to unexpected friction. It is believed that this extra friction and asymmetric behavior can be eliminated if the void between the internal shaft and the sleeve is appropriately enlarged.

Fig. 12(a) shows the typical strain gauge readings of the external tube. The maximum microstrain  $\varepsilon_\mu$  is significantly lower than the yield strain of 45# steel (nominal  $f_y = 355$  MPa, corresponding to yield strain of  $\varepsilon_\mu = 1,770$ ), which confirms the elastic behavior of the external tube. It is also noticed that the strain of the external tube is always close to zero when the device is in compression (negative load). This can be explained by the working mechanism shown in Fig. 2(b), which demonstrates that the load is not transferred to the

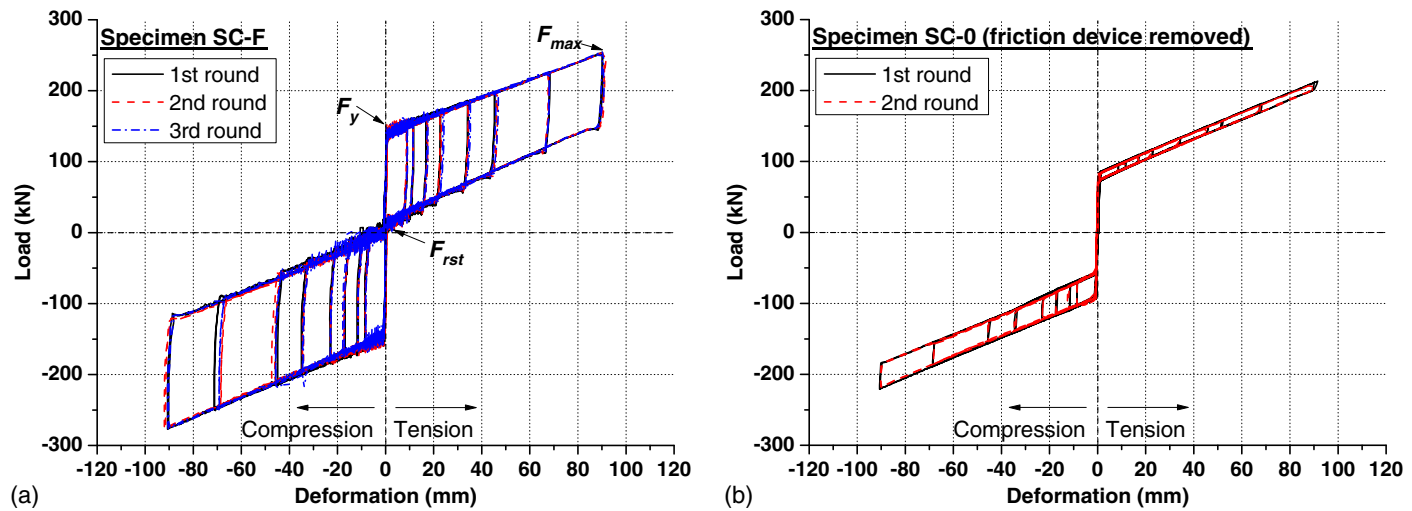


**Fig. 11.** Load-deformation hysteretic responses of device specimen: (a) SC-F; and (b) SC-0.

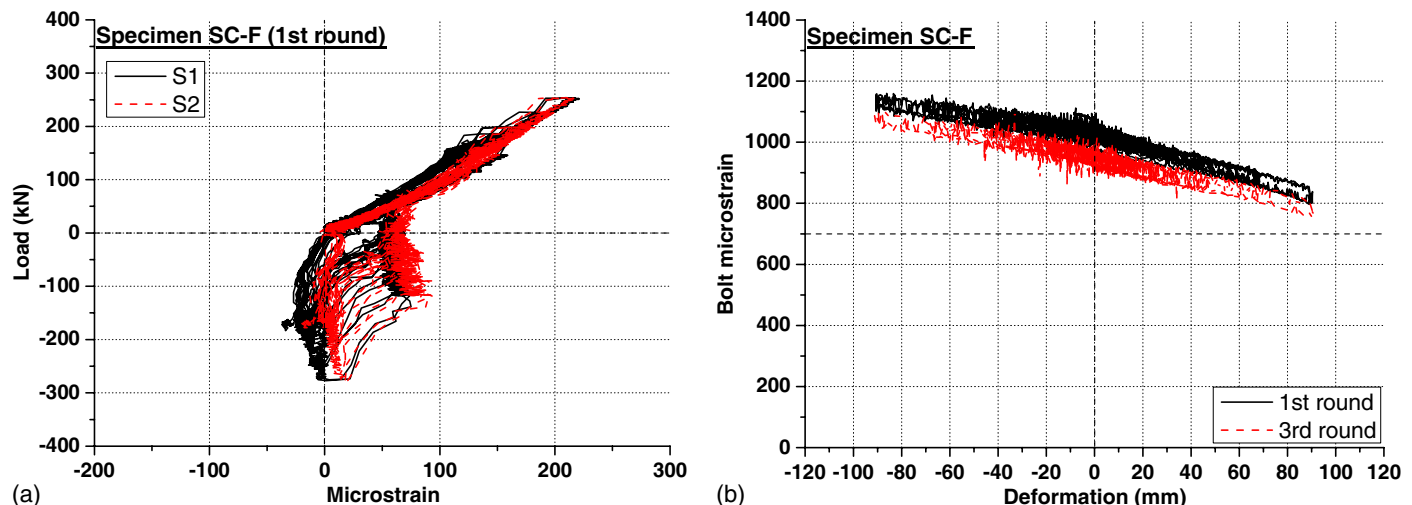


**Fig. 12.** Strain gauge readings: (a) outer tube strain; and (b) bolt strain.

external tube under this particular loading condition. Fig. 12(b) shows the variation of the typical bolt strain as the cycle is accumulated. It can be seen that the level of bolt strain gradually decreases. For example, compared with the average value during the first round of loading, the bolt strain is decreased by approximately 5% in the third round. As mentioned, this decrease was caused by the abrasion of the friction material. However, as the friction coefficient increases, the decrease in the bolt load seems to have little influence on the overall frictional force. The inconsistent bolt strain

when the device is tension and compression is attributed to the slightly bending behavior of the high-strength bolt when subjected to load reversal.

### Discussion of Test Results

Table 2 summarizes in more detail the basic characteristics of the specimens. The yield load ( $F_y$ ) of Specimen SC-F is approximately 140 kN and that of Specimen SC-0 is 83 kN on average.

**Table 2.** Summary of device test results

Test code	Test round	Yield load, $F_y$ (kN)	Maximum load, $F_{\max}$ <sup>a</sup> (kN)	Static initial stiffness, $K_{i-s}$ (kN/mm)	Dynamic initial stiffness, $K_{i-d}$ (kN/mm)	Postyield stiffness, $K_p$ (kN/mm)	Restoring force, $F_{rst}$ <sup>a</sup> (kN)	Energy dissipation, $W_D$ <sup>a</sup> (kJ)	EV <sup>a</sup> (%)
SC-F	1st	139.3	254.0	584.7	278.9	1.40	14.1	22.8	16.1
	2nd	138.4	254.5	618.1	285.5	1.39	15.1	22.8	15.8
	3rd	139.2	255.0	541.7	283.8	1.44	14.0	22.4	17.2
SC-0	1st	83.7	213.2	—	292.0	1.45	73.2	3.8	3.1
	2nd	82.6	208.9	—	236.0	1.43	74.1	3.7	3.1

<sup>a</sup>Typical values at the  $\pm 90$  mm cycle.

This indicates that the disc springs contribute to around 60% of the total yield resistance, and the remaining 40% is offered by the friction ED. For Specimen SC-F, the maximum load resistance ( $F_{\max}$ ) at  $\pm 90$  mm deformation is 254.5 kN on average, corresponding to a maximum-to-yield strength ratio, i.e.,  $F_{\max}/F_y$  ratio, of 1.82. This is a pronounced overstrength, which is, in fact, a beneficial characteristic for avoiding soft story mechanisms, especially at large interstory drifts when the  $P-\Delta$  effect becomes significant (Gupta and Krawinkler 1999). Cautions should be exercised that an increase in the maximum-to-yield strength ratio leads to increased load resistance demand for the adjacent members and connections, which should be carefully designed. Given the considered reservation of deformation for the present specimen, a maximum-to-yield strength ratio of at least 2.5 is recommended for the design of the members and connections. Both  $F_y$  and  $F_{\max}$  show little sensitivity to the repeated rounds of cyclic loading.

The stiffness response of the proposed device can be evaluated by either static stiffness ( $K_{i-s}$ ) or dynamic stiffness ( $K_{i-d}$ ), as separately given in Table 2. The former corresponds to the static friction response, and the value can be obtained by observing the elastic load-deformation response of the specimen before the relative motion of the friction interface is triggered; the latter corresponds to the stage after the relative motion of the friction interface and is more representative of the initial stiffness response during seismic excitation. In other words, the static stiffness can be used for estimating structural resistance/stiffness against normal design loads, such as wind or frequently occurred earthquakes (FoE), whereas the dynamic stiffness is more suitable for nonlinear time-history analysis. It can be seen from Table 2 that for Specimen SC-F, the average measured static stiffness is 581.5 kN/mm, which is evidently larger than the dynamic stiffness (282.7 kN/mm on average). If the friction ED is removed (i.e., Specimen SC-0), the two stiffnesses would have no difference. In fact, the initial stiffness response of the proposed self-centering device is related to many factors, such as the level of disc spring precompression, level of tightening (when installing the second part of the external tube), elastic deformation of device components, and possible machining tolerance (e.g., uneven bearing surface). For many types of self-centering devices, the initial test stiffness being lower than the theoretical value has been frequently reported (Christopoulos et al. 2008; Erochko et al. 2015a; Xu et al. 2017a, b). Huang et al. (2020) concluded that the actual initial stiffness of PT-based self-centering systems is

difficult to predict using theoretical equations due to the uncertainties related to manufacturing and fabrication. Generally speaking, the current specimens exhibit a quite large initial stiffness, showing the effectiveness of the proposed detailing. Table 2 also gives the postyield stiffness ( $K_p$ ), which is essentially the loading stiffness of the disc spring groups after activation, i.e., Eq. (7). The  $K_p/K_{i-d}$  ratio is 0.5%, which is smaller than that of metallic dampers (including BRBs), in which such a ratio typically ranges between 2% and 5%. Again, the relatively small  $K_p/K_{i-d}$  ratio is because of the large initial stiffness of the device.

Fig. 13 shows the variations of absolute energy dissipation per cycle ( $W_D$ ) and equivalent viscous damping (EVD) of the specimen as a function of the loading cycle. The EVD is a dimension-independent index for describing the energy dissipation capacity of the device, as given

$$EVD = \frac{W_D}{4\pi W_E} \quad (11)$$

where  $W_E$  = strain energy stored in the corresponding linear elastic system undergoing the same maximum displacement. It can be seen that the energy dissipation per cycle increases as the amplitude increases, and the response is quite stable under the three repeated rounds of cyclic loading. This echoes the stable hysteretic curves shown in Fig. 11 and indicates that the energy dissipation was reliably provided under the considered loading sequences. An EVD of up to 36% is observed, and the value gradually decreases with increasing amplitudes. This tendency is related to the varying shapes of the hysteresis at different amplitudes, recalling that EVD is a dimension-independent but shape-dependent index. The specimen provides a minimum EVD of 15% throughout the tests. Importantly, the large EVDs induced at small amplitudes imply that the device could participate in energy dissipation at very small interstory drifts.

The self-centering capability of the specimen was provided by the restoring force of the disc springs and was also largely determined by the frictional force. The self-centering tendency/capability of a system is often indicated by the restoring force ( $F_{rst}$ ), as illustrated in Fig. 11, in which an increase in the  $F_{rst}$  indicates an increased self-centering tendency. In addition,  $F_{rst} > 0$  means that the system can be fully recovered with no static residual deformation, and  $F_{rst} < 0$  corresponds to a partial self-centering system with certain static residual deformation. It has been recognized from system-level analysis (Fang et al. 2018) that an overly large  $F_{rst}$

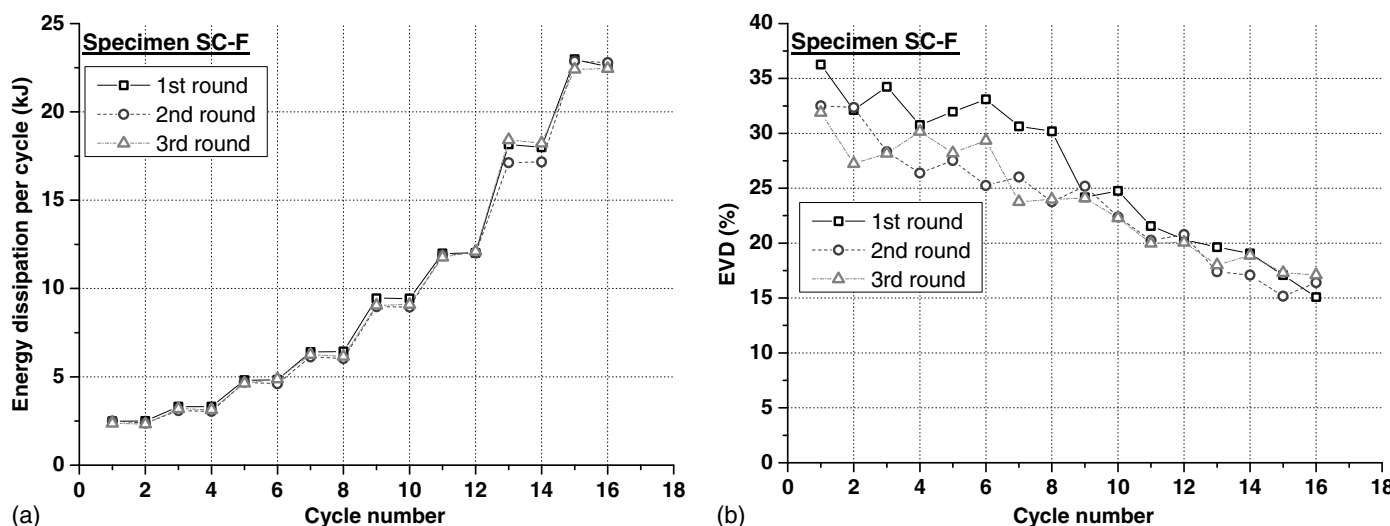


Fig. 13. Energy dissipation characteristics of device specimen: (a) absolute energy dissipation; and (b) EVD.

is not desirable as this would cause insufficient energy dissipation and, hence, increase the peak deformation response. For a high-rise building, an increase in  $F_{rst}$  could also lead to a detrimental high-mode effect and increased peak floor acceleration (Qiu and Zhu 2016). In other words, a trade-off between energy dissipation and self-centering capability should be made when designing self-centering devices. For the current specimen, the value of  $F_{rst}$  is close to zero and is not sensitive to the repeated loading. The device was just designed with the maximum possible energy dissipation without inducing any static residual deformation. In practice, the energy dissipation of the device and, hence, the shape of the hysteresis could be readily tuned by changing the preload of the high-strength bolts for the friction ED.

It is also worth mentioning that the self-centering capability of the device during quasi-static unloading can be largely different from that of the structural system experiencing dynamic shakedown during actual earthquake excitations (Eatherton and Hajjar 2011). An optimal design of the device may be obtained through a comprehensive system-level analysis; however, this is beyond the scope of this study.

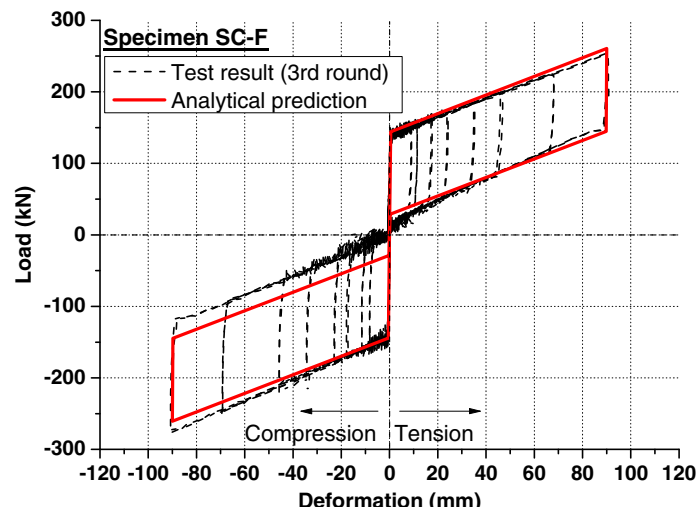
## Design Considerations

### Analytical Predictions

Keeping the basic working principle of the proposed device in mind, the flag-shaped hysteretic curve of the specimen can be conveniently predicted using the equations presented previously. The analytical predictions of Specimens SC-F and SC-0 are compared with the test results, as shown in Fig. 14, in which good agreements are observed. The small discrepancy could result from the inaccurate estimation of the overall friction action, recalling that extra friction was unexpectedly induced between the sleeve and the guiding tube when the specimen was in compression. Generally speaking, the analytical predictions can adequately capture the key characteristics of the hysteretic curve, and the predicted results are on the conservative side in terms of energy dissipation estimation.

### Parametric Study and Preliminary Design Recommendations

As limited variables were considered in the test program, the influences of precompression and friction are further understood by



extending the range of parameters. Fig. 15(a) shows the analytical predictions of the device with precompressions of 65 mm (the reference case which is identical with Specimen SC-F), 30 mm, and 0 mm. As the overall load resistance is contributed by both the preload and friction, decreasing the precompression leads to decreased yield resistance. The postyield stiffness and absolute energy dissipation are not affected, as the former depends on the elastic stiffness of the disc springs, and the latter is provided by the friction ED. The comparison of the results also highlights the fact that a sufficient preload needs to be applied to the disc springs in order to eliminate the residual deformation. Fig. 15(b) compares the response of the device with different frictional forces, namely, 0,  $F_f$  (reference case), and  $2F_f$ , where  $F_f = 58$  kN. As expected, increasing the friction tends to increase the load resistance and the area of the hysteresis. As aforementioned, one can trade self-centering capability for energy dissipation by increasing the friction, and a balance between the two characteristics should be maintained in practical design.

After gaining the necessary knowledge from the experimental and analytical investigations, it is suggested to have the following points in mind when conducting the design.

### Selection of Disc Springs Based on Performance Targets

Required yield resistance  $F_y$  and deformation demand are two performance targets that need to be determined at the beginning of the design. An energy dissipation factor,  $\beta$ , may be determined first, as marked in Fig. 15(a). This parameter describes the shape of the flag-shaped hysteretic loop, in which the device transforms from an elastic bilinear behavior (with no energy dissipation) to a full elastoplastic behavior when  $\beta$  increases from 0.0 to 2.0. For the proposed device,  $\beta$  can be expressed

$$\beta = \frac{2F_f}{F_y} = \frac{2F_f}{F_f + F_p} \quad (12)$$

Once  $F_y$  and  $\beta$  are determined, which are subjected to engineering judgment, the proportions of  $F_f$  and  $F_p$  are fixed, and their values are obtained. Empirically, a good starting point is to select a certain type of disc spring which, with an appropriate stacked number in parallel, provides the required  $F_p$  with a precompression of 30%–50% of the fully-flattened deformation. Eqs. (1)–(7) can be

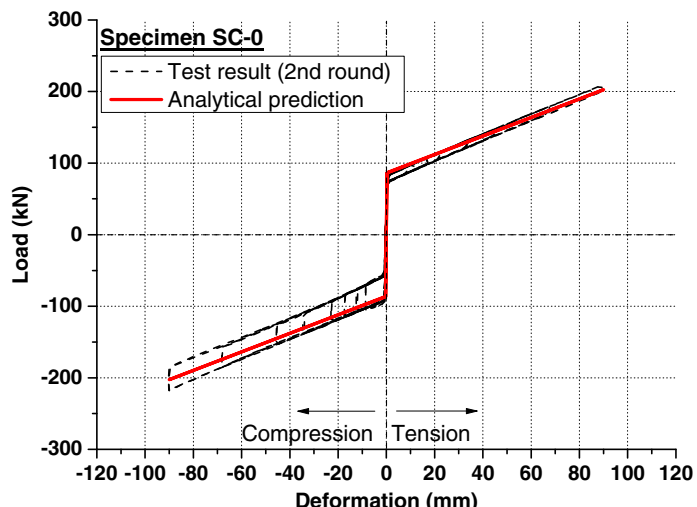


**Fig. 14.** Comparisons between test results and analytical predictions.

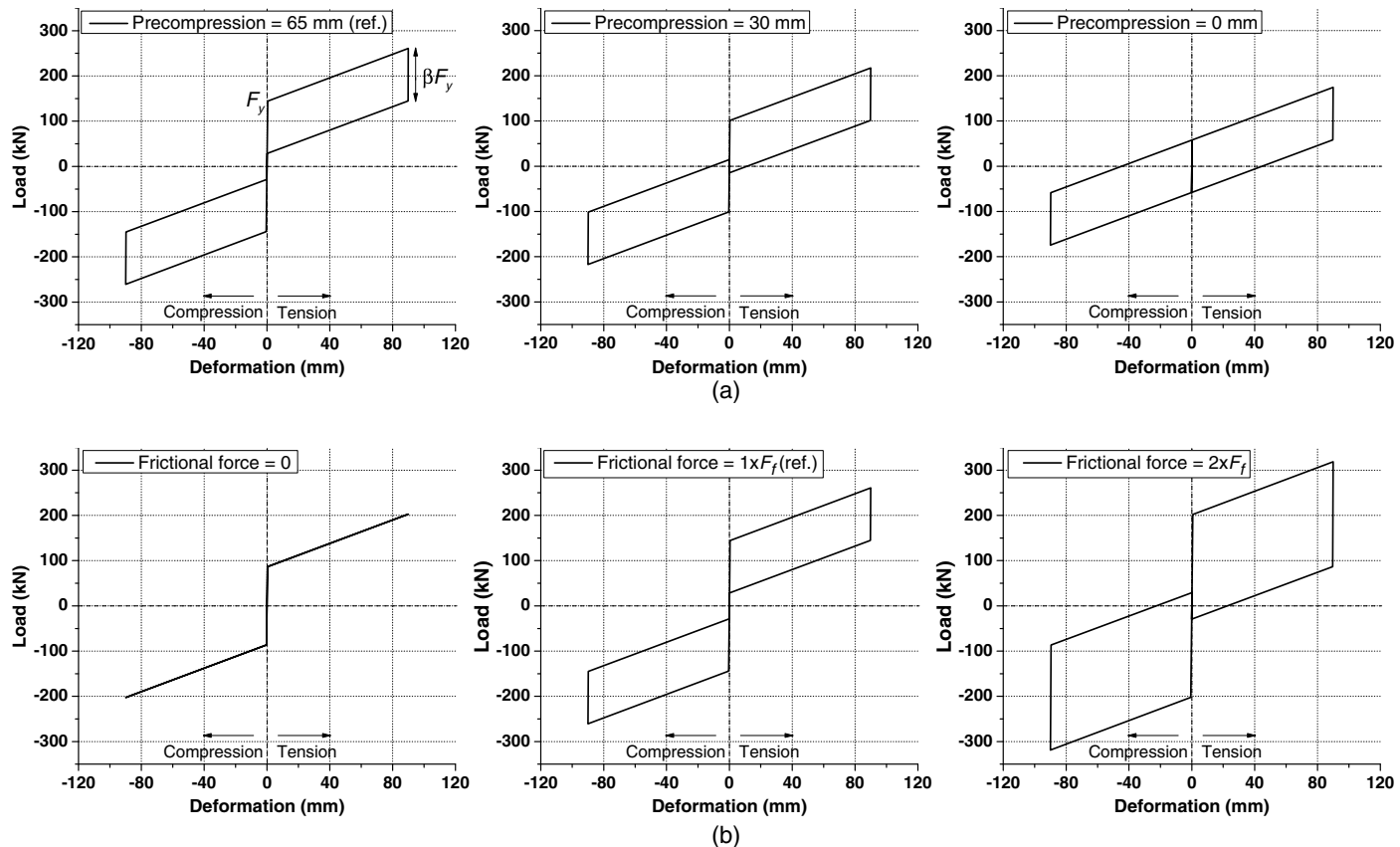


**Fig. 15.** Parametric study: (a) influence of precompression; and (b) influence of friction.

employed for such calculation. Meanwhile, an appropriate friction ED should be determined to provide the necessary  $F_f$ . Different combinations of the friction material, bolt torque, and bolt number can be adopted as long as the reliability of the friction ED is ensured (by either a field test or other quality control procedures). Subsequently, the required number of disc springs stacked in a series is selected according to the deformation demand, noting that precompression should be deducted from the available deformation. For example, according to ASCE/SEI 7-16 (ASCE 2016), the interstory drift limit of a building frame under the MCE is 4%, and hence, the minimum stroke of the device should be determined accordingly. The preceding process could be iterative.

### Design of Device

Once the arrangement of the disc springs is determined, the other components, such as the internal shaft, external tube, and sleeve, can be designed accordingly. These components should have yield resistance sufficiently larger than the maximum possible force provided by the disc springs plus the friction, and enough space to accommodate the stroke should be provided. In addition, the threaded joint should be strong enough, and the shim plates should remain elastic and have negligible bending deformation.

### Summary and Conclusions

This study has presented a new self-centering device, which is suitable for use in braced frames. The self-centering capability was provided by the preloaded disc springs, and energy dissipation was induced by extra friction. The study commenced with a

detailed description of the working principle and fabrication process of the proposed device, followed by a series of tests on individual disc springs, friction EDs, and, finally, a full-scale device specimen. Analytical expressions were also developed, which enabled a comprehensive description of the hysteretic behavior of the device. The analytical predictions were compared with the test results, after which further parametric analysis was carried out. The main findings and conclusions are summarized as follows:

- The three types of friction material, namely, nonasbestos carbon fiber composite (NCFC), nonasbestos aramid fiber composite (NAFC), and nonasbestos calcium sulfate whisker composite (NCSWC), generally provide reliable energy dissipation, although the friction coefficient tends to increase as the cycle is accumulated. NAFC is shown to provide the highest friction coefficient (up to 0.47) and a relatively stable hysteretic response.
- The device specimen showed typical flag-shaped hysteretic responses with anticipated mechanical behavior. The main deformation was provided by the disc springs, and the specimen can offer maximum deformability of at least 90 mm, corresponding to an interstory drift of 4%.
- The hysteretic response was very stable and insensitive to the repeated rounds of cyclic loading. Except for the minor abrasion of the friction material, no damage to any component was observed after completing the multiple rounds of testing, showing that the device was fully recoverable and reusable after undergoing sequential major earthquakes.
- The device specimen exhibited a relatively large initial stiffness, and the  $F_{\max}/F_y$  ratio was on average 1.82 at a 90-mm deformation. The large initial stiffness makes the device suitable for use in lateral resisting systems, such as braced frames, and the

- relatively high maximum-to-yield strength ratio helps prevent a weak story mechanism, although the adjacent members and connections should be designed accordingly.
- The device specimen showed excellent self-centering capability, and the energy dissipation capacity was reliably provided by the friction ED. A maximum equivalent viscous damping (EVD) of 36% was recorded, although the value decreases with increasing amplitudes. The device was expected to have sound energy dissipation capacity at both small and large interstory drifts.
  - The analytical expression well captured the hysteretic response of the device. A supplementary parametric study further revealed the influences of precompression and friction on the device behavior. The experiences gained from the experimental and analytical investigations finally lead to some preliminary design recommendations.

## Data Availability Statement

All data, models, and code generated or used during the study appear in the published article.

## Acknowledgments

Financial support from the National Natural Science Foundation of China (NSFC) with Grant Nos. 52078366, 51820105013, 51778456, and 51778459 are gratefully acknowledged. This study was also sponsored by Tongji Architectural Design (Group) Co. Ltd.

## References

- ASCE. 2016. *Minimum design loads for buildings and other structures*. ASCE/SEI 7-16. Reston, VA: ASCE.
- Bagheri, H., A. Hashemi, S. M. M. Yousef-Beik, P. Zarmani, and P. Quenneville. 2020. "New self-centering tension-only brace using resilient slip-friction joint: Experimental tests and numerical analysis." *J. Struct. Eng.* 146 (10): 04020219. [https://doi.org/10.1061/\(ASCE\)ST.1943-541X.0002789](https://doi.org/10.1061/(ASCE)ST.1943-541X.0002789).
- Chinese Standard. 2005. *Disc springs*. GB/T 1972-2005. Beijing: Chinese Standard.
- Chou, C. C., and J. H. Chen. 2011a. "Development of floor slab for steel post-tensioned self-centering moment frames." *J. Constr. Steel Res.* 67 (10): 1621–1635. <https://doi.org/10.1016/j.jcsr.2011.04.006>.
- Chou, C. C., and J. H. Chen. 2011b. "Seismic design and shake table tests of a steel post-tensioned self-centering moment frame with a slab accommodating frame expansion." *Earthquake Eng. Struct. Dyn.* 40 (11): 1241–1261. <https://doi.org/10.1002/eqe.1086>.
- Chou, C. C., Y. C. Chen, D. H. Pham, and V. M. Truong. 2014. "Steel braced frames with dual-core SCBs and sandwiched BRBs: Mechanics, modeling and seismic demands." *Eng. Struct.* 72: 26–40. <https://doi.org/10.1016/j.engstruct.2014.04.022>.
- Chou, C. C., T. H. Wu, A. R. O. Beato, P. T. Chung, and Y. C. Chen. 2016. "Seismic design and tests of a full-scale one-story one-bay steel frame with a dual-core self-centering brace." *Eng. Struct.* 111: 435–450. <https://doi.org/10.1016/j.engstruct.2015.12.007>.
- Chowdhury, M. A., A. Rahmzadeh, and M. S. Alam. 2019. "Improving the seismic performance of posttensioned self-centering connections using SMA angles or end plates with SMA bolts." *Smart Mater. Struct.* 28: 075044. <https://doi.org/10.1088/1361-665X/ab1ce6>.
- Christopoulos, C., R. Tremblay, H. J. Kim, and M. Lacerete. 2008. "Self-centering energy dissipative bracing system for the seismic resistance of structures: Development and validation." *J. Struct. Eng.* 134 (1): 96–107. [https://doi.org/10.1061/\(ASCE\)0733-9445\(2008\)134:1\(96\)](https://doi.org/10.1061/(ASCE)0733-9445(2008)134:1(96)).
- Dimopoulos, A. I., T. L. Karavasilis, G. Vasdravellis, and B. Uy. 2013. "Seismic design, modelling and assessment of self-centering steel frames using post-tensioned connections with web hourglass shape pins." *Bull. Earthquake Eng.* 11 (5): 1797–1816. <https://doi.org/10.1007/s10518-013-9437-4>.
- Dong, H., X. Du, Q. Han, H. Hao, K. Bi, and X. Wang. 2017. "Performance of an innovative self-centering buckling restrained brace for mitigating seismic responses of bridge structures with double-column piers." *Eng. Struct.* 148: 47–62. <https://doi.org/10.1016/j.engstruct.2017.06.011>.
- Eatherton, M. R., L. A. Fahnstock, and D. J. Miller. 2014. "Computational study of self-centering buckling-restrained braced frame seismic performance." *Earthquake Eng. Struct. Dyn.* 43: 1897–1914. <https://doi.org/10.1002/eqe.2428>.
- Eatherton, M. R., and J. F. Hajjar. 2011. "Residual drifts of self-centering systems including effects of ambient building resistance." *Earthquake Spectra* 27 (3): 719–744. <https://doi.org/10.1193/1.3605318>.
- Erochko, J., C. Christopoulos, and R. Tremblay. 2015a. "Design, testing, and detailed component modeling of a high-capacity self-centering energy-dissipative brace." *J. Struct. Eng.* 141 (8): 04014193. [https://doi.org/10.1061/\(ASCE\)ST.1943-541X.0001166](https://doi.org/10.1061/(ASCE)ST.1943-541X.0001166).
- Erochko, J., C. Christopoulos, and R. Tremblay. 2015b. "Design and testing of an enhanced-elongation telescoping self-centering energy-dissipative brace." *J. Struct. Eng.* 141 (6): 04014163. [https://doi.org/10.1061/\(ASCE\)ST.1943-541X.0001109](https://doi.org/10.1061/(ASCE)ST.1943-541X.0001109).
- Erochko, J., C. Christopoulos, R. Tremblay, and H. Choi. 2011. "Residual drift response of SMRFs and BRB frames in steel buildings designed according to ASCE 7-05." *J. Struct. Eng.* 137 (5): 589–599. [https://doi.org/10.1061/\(ASCE\)ST.1943-541X.0000296](https://doi.org/10.1061/(ASCE)ST.1943-541X.0000296).
- Erochko, J., C. Christopoulos, R. Tremblay, and H. J. Kim. 2013. "Shake table testing and numerical simulation of a self-centering energy dissipative braced frame." *Earthquake Eng. Struct. Dyn.* 42 (11): 1617–1635. <https://doi.org/10.1002/eqe.2290>.
- Fang, C., W. Wang, and W. Feng. 2019a. "Experimental and numerical studies on self-centring beam-to-column connections free from frame expansion." *Eng. Struct.* 198: 109526. <https://doi.org/10.1016/j.engstruct.2019.109526>.
- Fang, C., W. Wang, C. He, and Y. Y. Chen. 2017. "Self-centring behaviour of steel and steel-concrete composite connections equipped with NiTi SMA bolts." *Eng. Struct.* 150: 390–408. <https://doi.org/10.1016/j.engstruct.2017.07.067>.
- Fang, C., W. Wang, A. Zhang, R. Sause, J. Ricles, and Y. Chen. 2019b. "Behavior and design of self-centering energy dissipative devices equipped with superelastic SMA ring springs." *J. Struct. Eng.* 145 (10): 04019109. [https://doi.org/10.1061/\(ASCE\)ST.1943-541X.0002414](https://doi.org/10.1061/(ASCE)ST.1943-541X.0002414).
- Fang, C., M. C. H. Yam, A. C. C. Lam, and L. K. Xie. 2014. "Cyclic performance of extended end-plate connections equipped with shape memory alloy bolts." *J. Constr. Steel Res.* 94 (94): 122–136. <https://doi.org/10.1016/j.jcsr.2013.11.008>.
- Fang, C., M. C. H. Yam, A. C. C. Lam, and Y. Y. Zhang. 2015a. "Feasibility study of shape memory alloy ring spring systems for self-centring seismic resisting devices." *Smart Mater. Struct.* 24: 075024. <https://doi.org/10.1088/0964-1726/24/7/075024>.
- Fang, C., M. C. H. Yam, H. W. Ma, and K. F. Chung. 2015b. "Tests on superelastic Ni-Ti SMA bars under cyclic tension and direct-shear: Towards practical recentring connections." *Mater. Struct.* 48 (4): 1013–1030. <https://doi.org/10.1617/s11527-013-0212-4>.
- Fang, C., Q. Zhong, W. Wang, S. Hu, and C. Qiu. 2018. "Peak and residual responses of steel moment-resisting and braced frames under pulse-like near-fault earthquakes." *Eng. Struct.* 177: 579–597. <https://doi.org/10.1016/j.engstruct.2018.10.013>.
- Farmani, M. A., and M. Ghasssemieh. 2017. "Steel beam-to-column connections equipped with SMA tendons and energy dissipating devices including shear tabs or web hourglass pins." *J. Constr. Steel Res.* 135: 30–48. <https://doi.org/10.1016/j.jcsr.2017.04.003>.
- Feng, W., C. Fang, and W. Wang. 2019. "Behavior and design of top flange-rotated self-centering steel connections equipped with SMA ring spring dampers." *J. Constr. Steel Res.* 159: 315–329. <https://doi.org/10.1016/j.jcsr.2019.04.046>.
- Garlock, M. E. M., and J. Li. 2008. "Steel self-centering moment frames with collector beam floor diaphragms." *J. Constr. Steel Res.* 64 (5): 526–538. <https://doi.org/10.1016/j.jcsr.2007.10.006>.

- Gupta, A., and H. Krawinkler. 1999. *Seismic demands for performance evaluation of steel moment resisting frame structures (SAC Task 5.4.3)*. Rep. No. 132. Stanford, CA: Stanford Univ.
- Hashemi, A., S. M. M. Yousef-Beik, F. M. Darani, G. C. Clifton, P. Zarnani, and P. Quenneville. 2019. "Seismic performance of a damage avoidance self-centring brace with collapse prevention mechanism." *J. Constr. Steel Res.* 155: 273–285. <https://doi.org/10.1016/j.jcsr.2018.12.019>.
- Huang, Q., M. Dyanati, D. A. Roke, A. Chandra, and K. Sett. 2018. "Economic feasibility study of self-centering concentrically braced frame systems." *J. Struct. Eng.* 144 (8): 04018101. [https://doi.org/10.1061/\(ASCE\)ST.1943-541X.0002093](https://doi.org/10.1061/(ASCE)ST.1943-541X.0002093).
- Huang, X., M. R. Eatherton, and Z. Zhou. 2020. "Initial stiffness of self-centering systems and application to self-centering-beam moment-frames." *Eng. Struct.* 203: 109890. <https://doi.org/10.1016/j.engstruct.2019.109890>.
- Jiang, Z. Q., X. F. Yang, C. Dou, C. Li, and A. L. Zhang. 2019. "Cyclic testing of replaceable damper: Earthquake-resilient prefabricated column-flange beam-column joint." *Eng. Struct.* 183: 922–936. <https://doi.org/10.1016/j.engstruct.2019.01.060>.
- Kari, A., M. Ghassemieh, and S. A. Abolmaali. 2011. "A new dual bracing system for improving the seismic behavior of steel structures." *Smart Mater. Struct.* 20: 125020. <https://doi.org/10.1088/0964-1726/20/12/125020>.
- Ke, K., M. C. H. Yam, H. Zhang, A. C. C. Lam, and X. Zhou. 2020. "High strength steel frames with SMA connections in self-centring energy dissipation bays: Behaviour insights and a multi-mode-based nonlinear static procedure." *Smart Mater. Struct.* 29: 125020. <https://doi.org/10.1088/1361-665X/abc147>.
- Khoo, H. H., C. Clifton, J. Butterworth, and G. Macrae. 2013. "Experimental study of full-scale selfcentering sliding hinge joint connections with friction ring springs." *J. Earthquake Eng.* 17 (7): 972–997. <https://doi.org/10.1080/13632469.2013.787378>.
- Khoo, H. H., C. Clifton, J. Butterworth, G. Macrae, S. Gledhill, and G. Sidwell. 2012. "Development of the self-centering sliding hinge joint with friction ring springs." *J. Constr. Steel Res.* 78: 201–211. <https://doi.org/10.1016/j.jcsr.2012.07.006>.
- Kitayama, S., and M. C. Constantinou. 2017. "Fluidic self-centering devices as elements of seismically resistant structures: Description, testing, modeling, and model validation." *J. Struct. Eng.* 143 (7): 04017050. [https://doi.org/10.1061/\(ASCE\)ST.1943-541X.0001787](https://doi.org/10.1061/(ASCE)ST.1943-541X.0001787).
- Latour, M., G. Rizzano, A. Santiago, and L. S. da Silva. 2019. "Experimental response of a low-yielding, self-centering, rocking column base joint with friction dampers." *Soil Dyn. Earthquake Eng.* 116: 580–592. <https://doi.org/10.1016/j.soildyn.2018.10.011>.
- Lin, Y. C., R. Sause, and J. M. Ricles. 2013. "Seismic performance of a steel self-centering moment resisting frame: Hybrid simulations under design basis earthquake." *J. Struct. Eng.* 139 (11): 1823–1832. [https://doi.org/10.1061/\(ASCE\)ST.1943-541X.0000745](https://doi.org/10.1061/(ASCE)ST.1943-541X.0000745).
- McCormick, J., H. Aburano, M. Ikenaga, and M. Nakashima. 2008. "Permissible residual deformation levels for building structures considering both safety and human elements." In *Proc., 14th World Conf. Earthquake Engineering*. Beijing: Seismological Press of China.
- Miller, D. J., L. A. Fahnestock, and M. R. Eatherton. 2012. "Development and experimental validation of a nickel-titanium shape memory alloy self-centering buckling-restrained brace." *Eng. Struct.* 40 (Jul): 288–298. <https://doi.org/10.1016/j.engstruct.2012.02.037>.
- Moradi, S., M. S. Alam, and B. Asgarian. 2014. "Incremental dynamic analysis of steel frames equipped with NiTi shape memory alloy braces." *Struct. Des. Tall Spec. Build.* 23 (18): 1406–1425. <https://doi.org/10.1002/tal.1149>.
- Qiu, C., and S. Zhu. 2017a. "Performance-based seismic design of self-centering steel frames with SMA-based braces." *Eng. Struct.* 130 (Jan): 67–82. <https://doi.org/10.1016/j.engstruct.2016.09.051>.
- Qiu, C., and S. Zhu. 2017b. "Shake table test and numerical study of self-centering steel frame with SMA braces." *Earthquake Eng. Struct. Dyn.* 46 (1): 117–137. <https://doi.org/10.1002/eqe.2777>.
- Qiu, C. X., and S. Zhu. 2016. "High-mode effects on seismic performance of multi-story self-centering braced steel frames." *J. Constr. Steel Res.* 119 (Mar): 133–143. <https://doi.org/10.1016/j.jcsr.2015.12.008>.
- Ramhormozian, S., G. C. Clifton, G. A. MacRae, and G. P. Davet. 2017. "Stiffness-based approach for Belleville springs use in friction sliding structural connections." *J. Constr. Steel Res.* 138 (Nov): 340–356. <https://doi.org/10.1016/j.jcsr.2017.07.009>.
- Ramhormozian, S., G. C. Clifton, G. A. MacRae, G. P. Davet, and H. H. Khoo. 2019. "Experimental studies on Belleville springs use in the sliding hinge joint connection." *J. Constr. Steel Res.* 159 (Aug): 81–94. <https://doi.org/10.1016/j.jcsr.2019.03.031>.
- Ricles, J. M., R. Sause, M. Garlock, and C. Zhao. 2001. "Post-tensioned seismic resistant connections for steel frames." *J. Struct. Eng.* 127 (7): 113–121. [https://doi.org/10.1061/\(ASCE\)0733-9445\(2001\)127:2\(113\)](https://doi.org/10.1061/(ASCE)0733-9445(2001)127:2(113).
- Ricles, J. M., R. Sause, S. W. Peng, and L. W. Lu. 2002. "Experimental evaluation of earthquake resistant post-tensioned steel connections." *J. Struct. Eng.* 128 (7): 850–859. [https://doi.org/10.1061/\(ASCE\)0733-9445\(2002\)128:7\(850\)](https://doi.org/10.1061/(ASCE)0733-9445(2002)128:7(850).
- Tong, L., Y. Zhang, X. Zhou, A. Keivan, and R. Li. 2019. "Experimental and analytical investigation of D-type self-centering steel eccentrically braced frames with replaceable hysteretic damping devices." *J. Struct. Eng.* 145 (1): 04018229. [https://doi.org/10.1061/\(ASCE\)ST.1943-541X.0002235](https://doi.org/10.1061/(ASCE)ST.1943-541X.0002235).
- Tremblay, R., M. Lacerte, and C. Christopoulos. 2008. "Seismic response of multistory buildings with self-centering energy dissipative steel braces." *J. Struct. Eng.* 134 (1): 108–120. [https://doi.org/10.1061/\(ASCE\)0733-9445\(2008\)134:1\(108\)](https://doi.org/10.1061/(ASCE)0733-9445(2008)134:1(108).
- Wang, W., C. Fang, and J. Liu. 2016. "Large size superelastic SMA bars: heat treatment strategy, mechanical property and seismic application." *Smart Mater. Struct.* 25 (7): 075001. <https://doi.org/10.1088/0964-1726/25/7/075001>.
- Wang, W., C. Fang, and J. Liu. 2017a. "Self-centering beam-to-column connections with combined superelastic SMA bolts and steel angles." *J. Struct. Eng.* 143 (2): 04016175. [https://doi.org/10.1061/\(ASCE\)ST.1943-541X.0001675](https://doi.org/10.1061/(ASCE)ST.1943-541X.0001675).
- Wang, W., C. Fang, X. Yang, Y. Y. Chen, J. Ricles, and R. Sause. 2017b. "Innovative use of a shape memory alloy ring spring system for self-centering connections." *Eng. Struct.* 153 (Dec): 503–515. <https://doi.org/10.1016/j.engstruct.2017.10.039>.
- Wang, W., C. Fang, A. Zhang, and X. Liu. 2019a. "Manufacturing and performance of a novel self-centring damper with SMA ring springs for seismic resilience." *Struct. Control Health Monit.* 26 (5): e2337. <https://doi.org/10.1002/stc.2337>.
- Wang, W., C. Fang, Y. Zhao, R. Sause, S. Hu, and J. Ricles. 2019b. "Self-centering friction spring dampers for seismic resilience." *Earthquake Eng. Struct. Dyn.* 48 (9): 1045–1065. <https://doi.org/10.1002/eqe.3174>.
- Wood, A., I. Noy, and M. Parker. 2016. "The Canterbury rebuild five years on from the Christchurch earthquake." *Reserve Bank N. Z. Bull.* 79 (3): 1–16.
- Wu, D., B. Zhao, and X. Lu. 2018. "Dynamic behavior of upgraded rocking wall-moment frames using an extended coupled-two-beam model." *Soil Dyn. Earthquake Eng.* 115: 365–377. <https://doi.org/10.1016/j.soildyn.2018.07.043>.
- Xu, L. H., X. W. Fan, and Z. X. Li. 2016a. "Development and experimental verification of a pre-pressed spring self-centering energy dissipation brace." *Eng. Struct.* 127: 49–61. <https://doi.org/10.1016/j.engstruct.2016.08.043>.
- Xu, L. H., X. W. Fan, and Z. X. Li. 2017a. "Cyclic behavior and failure mechanism of self-centering energy dissipation braces with pre-pressed combination disc springs." *Earthquake Eng. Struct. Dyn.* 46 (7): 1065–1080. <https://doi.org/10.1002/eqe.2844>.
- Xu, L. H., X. W. Fan, and Z. X. Li. 2017b. "Experimental behavior and analysis of self-centering steel brace with pre-pressed disc springs." *J. Constr. Steel Res.* 139: 363–373. <https://doi.org/10.1016/j.jcsr.2017.09.021>.
- Xu, L. H., X. W. Fan, and Z. X. Li. 2020. "Seismic assessment of buildings with prepressed spring self-centering energy dissipation braces." *J. Struct. Eng.* 146 (2): 04019190. [https://doi.org/10.1061/\(ASCE\)ST.1943-541X.0002493](https://doi.org/10.1061/(ASCE)ST.1943-541X.0002493).
- Xu, X., Y. Zhang, and Y. Luo. 2016b. "Self-centering eccentrically braced frames using shape memory alloy bolts and post-tensioned tendons." *J. Constr. Steel Res.* 125 (Oct): 190–204. <https://doi.org/10.1016/j.jcsr.2016.06.017>.

- Yam, M. C. H., C. Fang, A. C. C. Lam, and Y. Y. Zhang. 2015. "Numerical study and practical design of beam-to-column connections with shape memory alloys." *J. Constr. Steel Res.* 104: 177–192. <https://doi.org/10.1016/j.jcsr.2014.10.017>.
- Zhang, A. L., H. Zhang, Z. Q. Jiang, C. Li, and X. Liu. 2020. "Low cycle reciprocating tests of earthquake-resilient prefabricated column-flange beam-column joints with different connection forms." *J. Constr. Steel Res.* 164: 105771. <https://doi.org/10.1016/j.jcsr.2019.105771>.
- Zhu, S., and Y. Zhang. 2008. "Seismic analysis of concentrically braced frame systems with self-centering friction damping braces." *J. Struct. Eng.* 134 (1): 121–131. [https://doi.org/10.1061/\(ASCE\)0733-9445\(2008\)134:1\(121\)](https://doi.org/10.1061/(ASCE)0733-9445(2008)134:1(121)).